NACA

RESEARCH MEMORANDUM

EFFECT OF THROAT BLEED ON THE SUPERSONIC PERFORMANCE OF A HALF-CONICAL SIDE-INLET SYSTEM

By Leonard E. Stitt, Frank X. McKevitt, and Albert B. Smith

Lewis Flight Propulsion Laboratory
Cleveland, Ohio

NATIONAL ADVISORY COMMITTEE
FOR AERONAUTICS

WASHINGTON

January 10, 1956

NATIONAL ADVISORY COMMITTEE FOR AERONAUTICS

RESEARCH MEMORANDUM

EFFECT OF THROAT BLEED ON THE SUPERSONIC PERFORMANCE OF A HALF-CONICAL SIDE-INLET SYSTEM

By Leonard E. Stitt, Frank X. McKevitt
and Albert B. Smith

SUMMARY

An experimental investigation was conducted at Mach numbers of 2.0, 1.8, and 1.5 to determine the effects of several throat boundary-layer bleed configurations on the performance of a 25° half-conical side-inlet system. The effects of several flush-slot configurations and a porous-surface bleed were determined over ranges of angle of attack and bleed-duct and main-duct mass flow. At Mach number 2.0, a flush-slot system showed an increase in propulsive thrust of 4 percentage points over the no-bleed configuration. The various bleed systems tested did not, in general, reduce the total-pressure distortions at the diffuser exit but did decrease the stable subcritical inlet-mass-flow range.

INTRODUCTION

Removal of the compression-surface boundary layer at the throat of a supersonic diffuser may offer increases in total-pressure recovery sufficient to outweigh the drag penalties that this bleed system might impose (refs. 1 and 2). Also a half-cone on-fuselage configuration is an efficient side inlet provided that ample provision is made to prevent the entry of the fuselage boundary layer into the ducts (ref. 3). These features were incorporated in a proposed supersonic airplane, a one-sixth scale model of which was tested in the Lewis 8- by 6-foot supersonic wind tunnel. Both porous-material and flush slots were used as throat bleeds. For comparison, a no-bleed inlet was also tested. The results of this investigation, for ranges of angle of attack and main-duct and bleed-duct mass flow at Mach numbers of 2.0, 1,8, and 1.5, are reported herein.

SYMBOLS

The following symbols are used in this report:

A	area
C_{D_a}	axial-force coefficient, D_a/q_0A_f
D_a	axial force
ΔD_a	increment of axial force between minimum and operating point
D_s	drag associated with discharging bleed flow through a sonic exit parallel to free-stream direction
F_n	engine thrust at diffuser total-pressure recovery
$F_{n,i}$	engine thrust at 100-percent diffuser total-pressure recovery
L	length of subsonic diffuser, 38.2 in.
l	length of nose ahead of flow survey station, 40.6 in.
M	Mach number
m	mass flow
P	total pressure
P'	pitot pressure
p	static pressure
q	dynamic pressure, $\gamma pM^2/2$
v	velocity
W	weight flow
x	distance from cowl lip
y	distance normal to fuselage
α	angle of attack with respect to fuselage reference line
γ	specific heat of air, 1.4
δ	ratio of total pressure to NACA standard sea-level pressure of 2116 lb/sq ft

3874

θ ratio of total temperature to NACA standard sea-level temperature of 518.7° R

θ_l cowl-lip parameter, angle in degrees between cone tip and cowl lip

Φ angle of local flow with respect to inlet centerline

Subscripts:

0 free-stream

1 conditions at flow survey station 40.6

3 conditions at diffuser-exit survey station 71.1

b bleed

x conditions at x distance from cowl lip

Pertinent Areas:

A_f maximum frontal cross-sectional area, 0.663 sq ft

A_i projected cowl-lip area of both inlets, 0.129 sq ft for $\theta_l = 40°$, 0.151 sq ft for $\theta_l = 38°$

A_3 diffuser-exit area, 0.161 sq ft

APPARATUS AND PROCEDURE

The one-sixth scale twin-duct fuselage forebody model used in this investigation (fig. 1) was mounted through an internal strain-gage balance to a strut in the Lewis 8- by 6-foot supersonic wind tunnel. An extension to the fuselage was connected to the sting but was mechanically independent of the model and balance. This extension was used to protect the various actuating mechanisms and the instrumentation at the rear of the model. Also on the extension were four reverse scoops (one of which is visible above the left inlet in fig. 1) used to lower the pressure at the base of the model and to ensure choking of the mass-flow control plugs.

Details of the model including representative cross sections, the internal ducting, the positions of the remotely actuated mass-flow control plugs, the $2\frac{1}{2}°$ fuselage nose droop, and the 4° downward inlet cant are shown in figure 2.

The inlet details of the various configurations tested are shown in figures 3 and 4. All configurations tested had the inlet compression cone mounted directly on the fuselage with the cone undercut from its apex to the inboard cowl lip. This undercut faired smoothly into the fuselage boundary-layer diverter wall. The inlet was wrapped around the fuselage in order to maintain a constant fuselage boundary-layer removal height of $1\frac{1}{2}$ times the estimated boundary-layer thickness. This height was based on the results of reference 3, which did not include throat bleed. The no-bleed and porous-surface bleed inlets were geometrically similar, the only difference being the addition of the porous surface. The location of this porous material is indicated in figure 4(a) as a shaded area. The first throat flush slot tested is illustrated in figure 4(b). Another cone and cowl block were used for the inlet with the 38° cowl-lip parameter θ_l. With this inlet, two positions of the throat-bleed slot were tested. After the initial run, the slot was moved 1/2 inch rearward to obtain the more gentle curvature shown in figure 4(c). The bleed flow, which discharged at the base of the model, was regulated by plugs (as seen in fig. 2).

Instrumentation for the flow survey ahead of the inlet (station 40.6) consisted of two 6° half-angle wedge bars on the left side of the fuselage for obtaining the local Mach number and the local flow angle. On the right side, at the same station, were three rakes, each consisting of nine total-pressure tubes and one static-pressure tube. These rakes were used to determine the fuselage boundary-layer thickness and, in conjunction with the wedge data, to detect any total-pressure loss ahead of the inlet. The model was also tested with 18 total-pressure tubes and two static-pressure tubes placed in each inlet cowl at station 46.7. These rakes were used for the determination of the inlet total-pressure contours, and were removed for the general data presented herein. Two dynamic pickups were located in the subsonic diffuser in order to detect static-pressure fluctuations.

The diffuser-exit rakes (fig. 2, station 71.1) were located at the point where the two ducts joined into a common duct. The six radial rakes consisted of six total-pressure tubes each. These tubes were located at the centroids of equal areas. Also located at this station were twelve wall static-pressure tubes, one at the end of each rake. At model station 75.00, the mass-flow measuring station, were located eight wall static-pressure tubes equally spaced - four on the centerbody and four on the outer duct wall. In computing the mass-flow ratio at this station, the flow was assumed to be choked at the geometric minimum area determined by the mass-flow-control-plug setting. The diffuser total-pressure recovery was computed using this mass flow and the static pressure ahead of the rake station.

The subsonic-diffuser area-variation curves are presented in figure 5. The positions of the measuring stations and some representative duct cross sections are indicated. These curves are for faired cones, that is, the increase in area caused by the bleed slots is not included.

The bleed-duct system performance was determined with the use of four total-pressure and two static-pressure tubes in each of the two bleed-discharge ducts (station 71.6).

Only the model axial force was measured by the internal strain-gage balance. The axial-force coefficient presented excludes the base pressure forces and the thrust forces produced by both the main-duct and the bleed-duct flows. The duct thrusts were defined as the change in momentum from the free stream to the duct exit.

The investigation was conducted at free-stream Mach numbers of 1.5, 1.8, and 2.0 over a range of bleed-duct and main-duct mass flows and angles of attack. The Reynolds number range for the test was 4.1×10^6 to 5.3×10^6 per foot.

RESULTS AND DISCUSSION

The flow conditions ahead of the inlets are presented in figure 6. At a free-stream Mach number of 2.0, the local flow is nearly alined with the inlet when the model is at an angle of attack of 2° (fig. 6(a)). The general increase in local Mach number ahead of the inlet over free-stream Mach number and its variation between wedge positions due to the nose and canopy is also shown. The pitot-pressure-ratio curves show the boundary-layer profile including the estimated thickness. When the pitot-pressure recovery is compared with normal-shock recovery at the indicated local Mach number, no significant loss in total pressure ahead of the inlet is apparent. The boundary-layer-removal height was nearly 1.5 times the boundary-layer thickness as estimated.

The flow field with the canopy removed and the nose faired over (see fig. 2) is shown in figure 6(b). A comparison of figure 6(a) with 6(b) indicates that the addition of the canopy increased the local Mach number, particularly in the region of the upper wedge. However, the boundary-layer thickness was virtually unaffected.

The performance curves for the configurations are presented in figure 7. The performance parameters are plotted against engine mass flow, which differs from inlet flow by the amount of bleed-duct flow. The mass-flow ratios were referenced to the projected cowl-lip area and, since the cone tip was on the fuselage (fig. 4(a)), values of supercritical mass-flow ratio greater than unity theoretically could be and experimentally were obtained. On these figures a flagged symbol is used

to indicate the minimum stable mass flow, defined as the lowest mass flow reached before the full amplitude of the static-pressure fluctuations in the duct exceeded 5 percent of the free-stream total pressure. The minimum mass flow presented at Mach number 1.5 represents the limit of the mass-flow-control-plug travel, and all inlets were stable to this limit. Lines of constant corrected air flow are indicated on all internal performance curves. At any given Mach number the performance remained essentially constant for angles of attack of -2° to 2°. At angles above 5° the internal performance decreased rapidly. At zero angle of attack, the minimum axial-force coefficient increased with decreasing values of free-stream Mach number.

The performance characteristics for the first position of the internal flush slot for the inlet with $\theta_l = 38^\circ$ is presented in figure 7(d). A variation in the longitudinal position of the flush slot (fig. 4(c)) for this inlet had no discernable effect on the performance; therefore, the data for the second position are not presented.

The variation in performance obtained at cruise angle of attack ($\alpha = 2^\circ$) with changes in bleed configuration is more apparent in the summary plot (fig. 8). For the purpose of external drag comparison, these data are plotted against total inlet-mass-flow ratio (engine mass flow plus bleed-duct mass flow). The porous-surface and flush-slot inlets show an increase in maximum total-pressure recovery over the no-bleed inlet at all Mach numbers.

From optical observations, it was apparent that the regions of rapidly decreasing pressure recovery at reduced mass flows were caused by asymmetrical operation of the twin-duct system. When the mass-flow ratio was reduced, the $\theta_l = 38^\circ$ bleed inlet maintained the high pressure recovery farther into the subcritical region. This would be expected since, with the oblique shock farther ahead of the cowl lip, the normal-shock recovery air would not enter the cowl until a lower value of mass flow was reached.

All the bleed configurations showed a decrease in stable subcritical inlet-mass-flow range when compared with the no-bleed inlet. At Mach numbers 2.0 and 1.8 the onset of instability, however, occurred at comparable engine mass flows (inlet mass flow minus bleed mass flow).

The curves presented in figure 9 represent the optimum inlet operating point for each Mach number and includes (1) the ratio of engine thrust for the given total-pressure recovery F_n to the engine thrust of a present day engine at an altitude of 35,000 feet and 100 percent pressure recovery $F_{n,i}$; (2) the drag D_s associated with discharging the bleed air from a sonic exit parallel to the free-stream direction (this drag may be pessimistic since the pressure recovery used in the calculation was the value measured in the test which was low because of the

dumping losses); (3) the difference between the minimum axial-force coefficient indicated on figure 8 and the operating point of the inlet ΔD_a. Although the flush-slot $\theta_l = 38^\circ$ inlet showed the highest pressure recovery, the propulsive-thrust evaluation showed the flush-slot $\theta_l = 40^\circ$ inlet to be superior over most of the test range. At Mach number 2.0, the propulsive thrust was increased 4 percentage points by the use of internal throat-bleed slots. The lower thrust-minus-drag performance of the $\theta_l = 38^\circ$ inlet was caused by the higher axial force produced by the larger cowl used with this configuration.

At Mach numbers 2.0 and 1.8, internal bleed reduced the magnitude of the diffuser static-pressure fluctuations in the mass-flow range above the minimum stable point (fig. 10). The fairing of the curves between data points was guided by static-pressure traces obtained continuously during control-plug travel. The arrows indicate the point where the amplitude was significantly greater than 5 percent of free-stream total pressure. No data were taken below this mass flow in order to avoid any damage to the balance linkage. Pressure traces (not presented) indicated pressure fluctuations of less than 2 percent for the porous-surface inlet at all Mach numbers and less than 1 percent at Mach number 1.5 for all the inlets over the given range of mass flow and angle of attack.

The asymmetrical operation of the inlets at Mach number 2.0 is apparent in the schlieren photographs (fig. 11). These photographs cover a range of mass flow for both of the flush-slot inlets, $\theta_l = 40^\circ$ and 38°. The first photograph for each inlet represents the point of peak recovery. For the $\theta_l = 40^\circ$ inlet all the subcritical spillage was from one inlet, the other remaining supercritical throughout the entire mass-flow range. Subcritical operation was obtained with both inlets for a limited mass-flow range for the inlet $\theta_l = 38^\circ$ configuration. At very low mass flows, however, with this inlet the spillage again took place from one side only.

Inlet and diffuser-exit total-pressure contours (fig. 12) are shown for ranges of mass flow, angle of attack, and free-stream Mach number. Since the external configurations were identical, the inlet contours obtained without bleed are presented with exit contours obtained with the $\theta_l = 40^\circ$ flush-slot inlet. The points were matched at comparable total inlet mass flows. Near critical mass flow at Mach number 2.0 (fig. 12(a)), the general level of the inlet recovery is near theoretical, but local areas of higher than theoretical recovery (for this configuration) indicate multishock compression due to shock - boundary-layer interaction. The asymmetrical operation of the inlets at low mass flows is apparent in figure 12(b). Boundary-layer thickening and flow separations in the leeward areas at the inlet station occurred at an angle of attack of 10° (figs. 12(c) and (d)). For points near critical mass flow at Mach numbers 1.8 and 1.5 (figs. 12(e) and (g), respectively), the inlet flow is

symmetrical and the total-pressure recovery is near theoretical for this configuration. Regions of high recovery at the inlet did not, in general, carry straight back to corresponding positions at the diffuser exit. The asymmetry of the inlet flow at Mach 1.8 (fig. 12(f)) is reversed from that at Mach 2.0 (fig. 12(b)). Here the left inlet is operating at or near critical; whereas in the right inlet there are two distinct regions of compression. The level of recovery near the outer cowl lip is approximately equal to normal-shock recovery; whereas the remainder of the inlet face exhibits the high recovery associated with multishock compression. This familiar pattern is caused by the intersection of the oblique and normal shocks in front of the inlet at subcritical mass flows.

At a given corrected engine air flow (near critical), the various bleed systems raised the level of recovery, but did not, in general, reduce the total-pressure distortions at the diffuser exit (fig. 13). Although these contours are for the same diffuser-exit Mach number, the external shock structures were slightly different because of different inlet mass flows. Diffuser-exit distortions are defined as the ratio, in percent, of the difference between maximum and minimum local total pressure to the duct average total pressure. The minimum total pressure used in the calculation was the lowest value that was measured at the exit rakes. These values of distortion are plotted over a range of corrected engine air flow (fig. 14). At the given angles of attack, a decreasing trend with decreasing air flow is indicated until the onset of twin-duct asymmetry. At this point there is a marked increase in the distortion level. A further reduction in the air flow, if pulsing was not encountered, again resulted in decreasing flow distortions in most cases. At an angle of attack of 10°, in the symmetrical flow region the general level of distortion increased slightly for all inlets.

The effect of bleed-duct mass flow on the performance of flush-slot inlet, for $\theta_l = 38^{\circ}$ and zero angle of attack is presented in figure 15. For Mach number 2.0 at a constant corrected engine air flow (with the inlet operating subcritical) 6 percent bleed flow was required to obtain maximum recovery. The recovery increased from 0.83 with no bleed to 0.88 with optimum bleed. As the bleed flow increased, the normal shock approached the cowl lip and the inlet mass-flow ratio increase resulted in reduced normal-shock spillage drag. At the two lower Mach numbers the gains in total-pressure recovery were not as large as those obtained at Mach number 2.0. Moreover, a greater amount of bleed-duct mass flow was required to obtain optimum recovery.

Only the total-pressure recovery and the drag associated with discharging the various amounts of bleed-duct mass flow were considered in preparing a propulsive-thrust curve for the $\theta_l = 38^{\circ}$ inlet (fig. 16). The total-pressure recoveries were taken directly from figure 15, and the bleed-duct discharge drag was computed from the following equation

$$D_s = m_b(v_0 - v_b) - (p_b - p_0)A_b$$

At Mach number 2.0, optimum propulsive thrust was obtained with about 6 percent bleed flow. At Mach numbers 1.8 and 1.5, the gains in propulsive thrust with bleed were much less than those obtained at Mach number 2.0.

SUMMARY OF RESULTS

An experimental investigation to evaluate the effects of several throat bleed configurations on the performance of a half-conical side-inlet system yielded the following results:

1. At a free-stream Mach number of 2.0, the propulsive thrust was increased 4 percentage points when a flush-slot air bleed was added to the inlet throat.

2. The various bleed systems increased the maximum pressure recovery over the no-bleed inlet, but did not, in general, reduce the pressure distortions at the diffuser exit.

3. All the bleed configurations tested showed a decrease in stable subcritical inlet-mass-flow range when compared with the no-bleed inlet. At Mach numbers 2.0 and 1.8, the onset of instability occurred at comparable engine mass flows (inlet mass flow minus bleed mass flow).

Lewis Flight Propulsion Laboratory
National Advisory Committee for Aeronautics
Cleveland, Ohio, October 7, 1955

REFERENCES

1. Obery, Leonard J., and Cubbison, Robert W.: Effectiveness of Boundary-Layer Removal Near Throat of Ramp-Type Side Inlet at Free-Stream Mach Number of 2.0. NACA RM E54I14, 1954.

2. Campbell, Robert C.: Performance of a Supersonic Ramp Inlet with Internal Boundary-Layer Scoop. NACA RM E54I01, 1954.

3. Piercy, Thomas G., and Johnson, Harry W.: A Comparison of Several Systems of Boundary-Layer Removal Ahead of a Typical Conical External-Compression Side Inlet at Mach Numbers of 1.88 and 2.93. NACA RM E53F16, 1953.

Figure 1. - Model in tunnel.

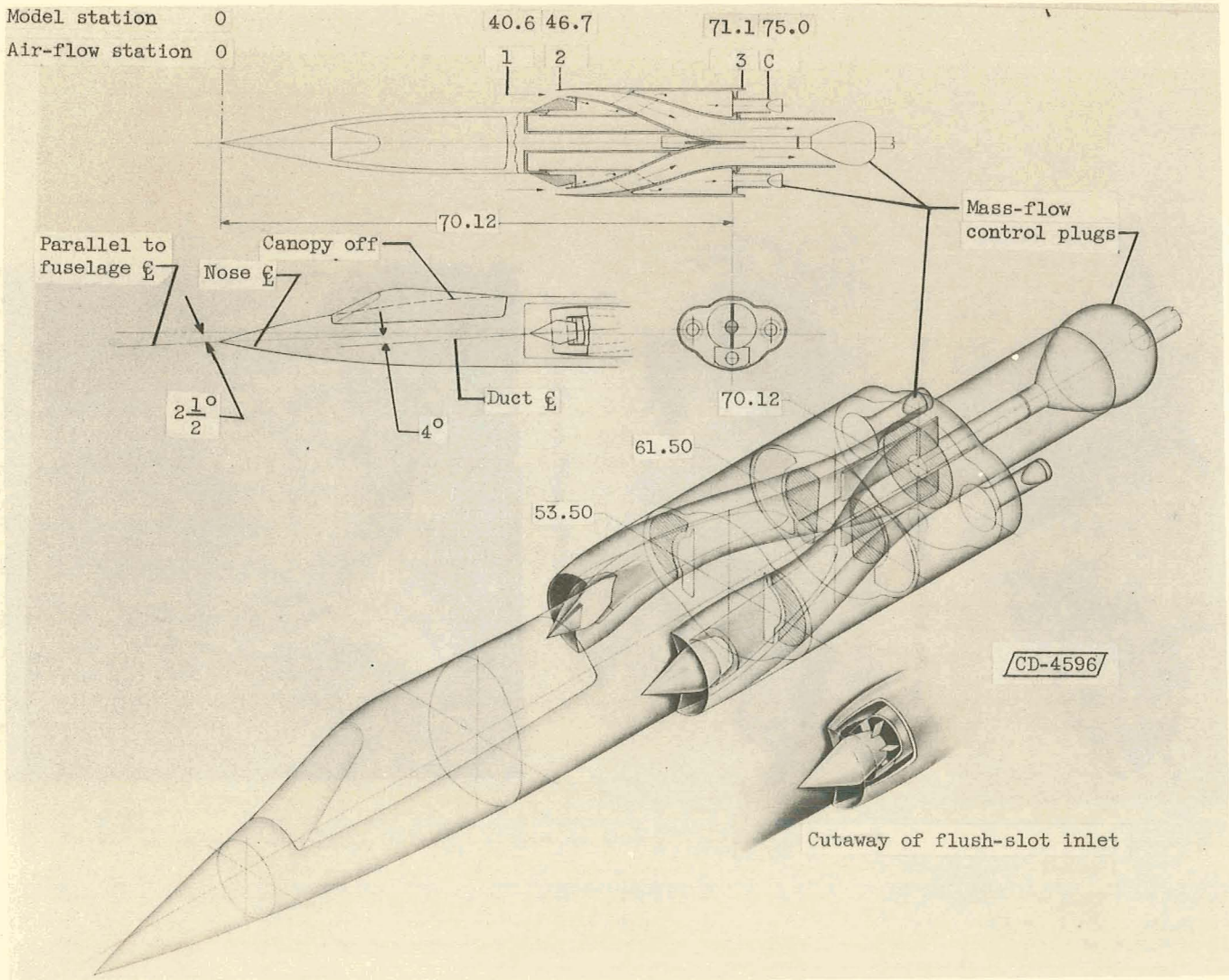

Figure 2. - Sketch of model with representative cross sections. (All dimensions in inches.)

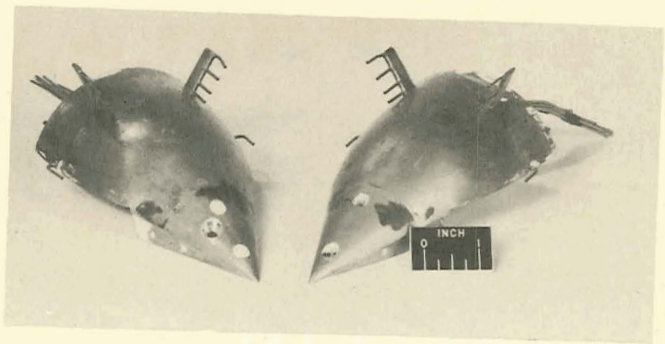

(a) No-bleed cones with inlet rakes.

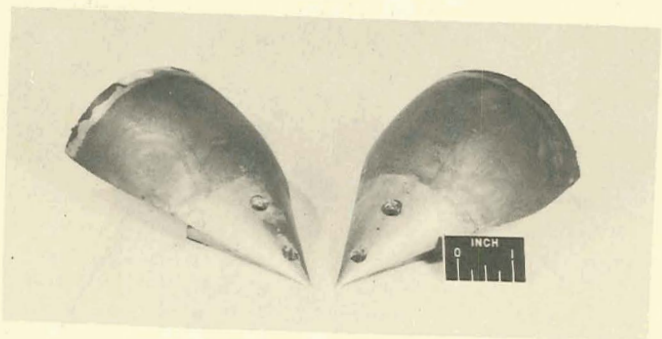

(b) Porous surface cones.

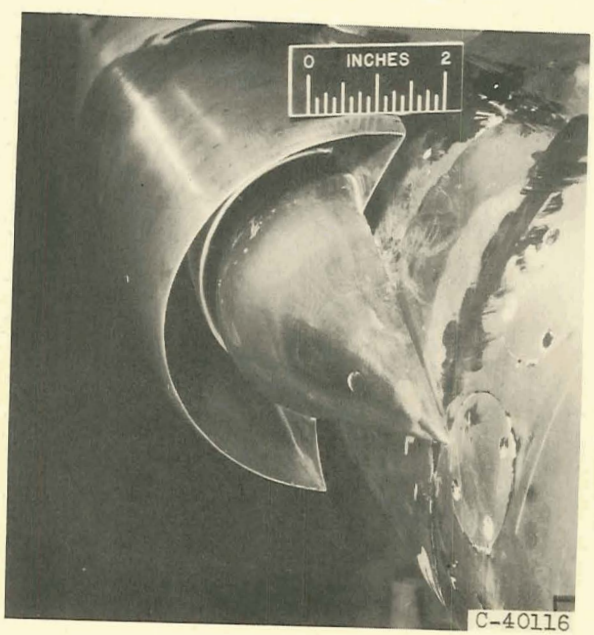

(c) Internal flush-slot inlet; cowl-lip parameter, 38°.

Figure 3. - Inlet components.

(a) No bleed and porous-surface bleed.

Figure 4. - Inlet configuration details.

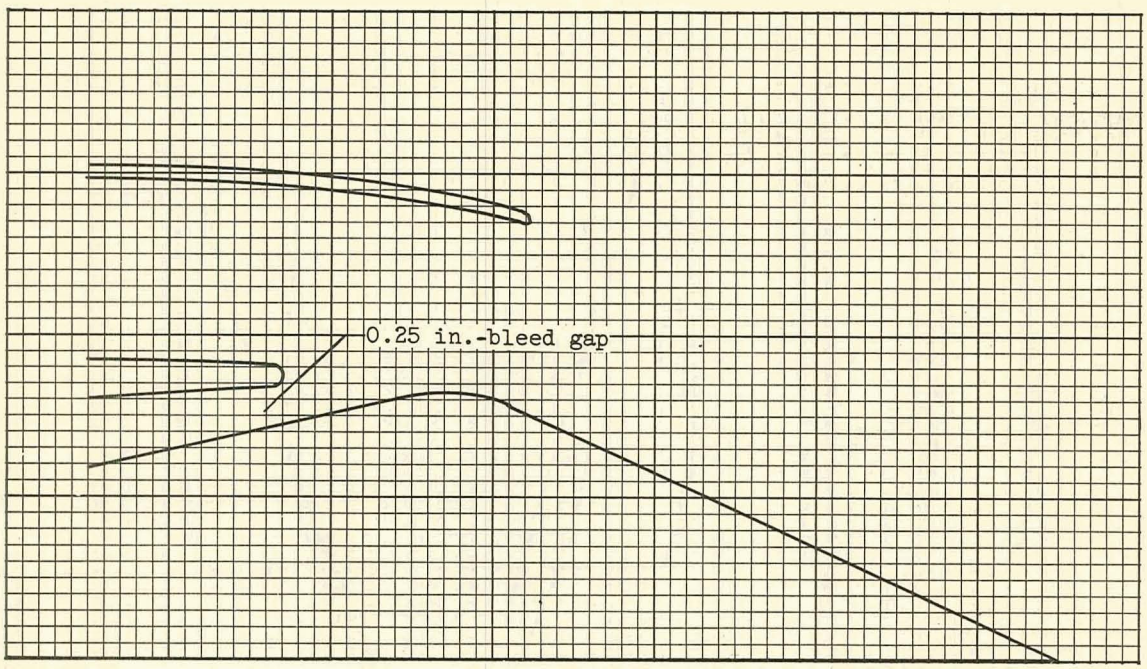

(b) Flush slot; cowl-lip parameter, 40°.

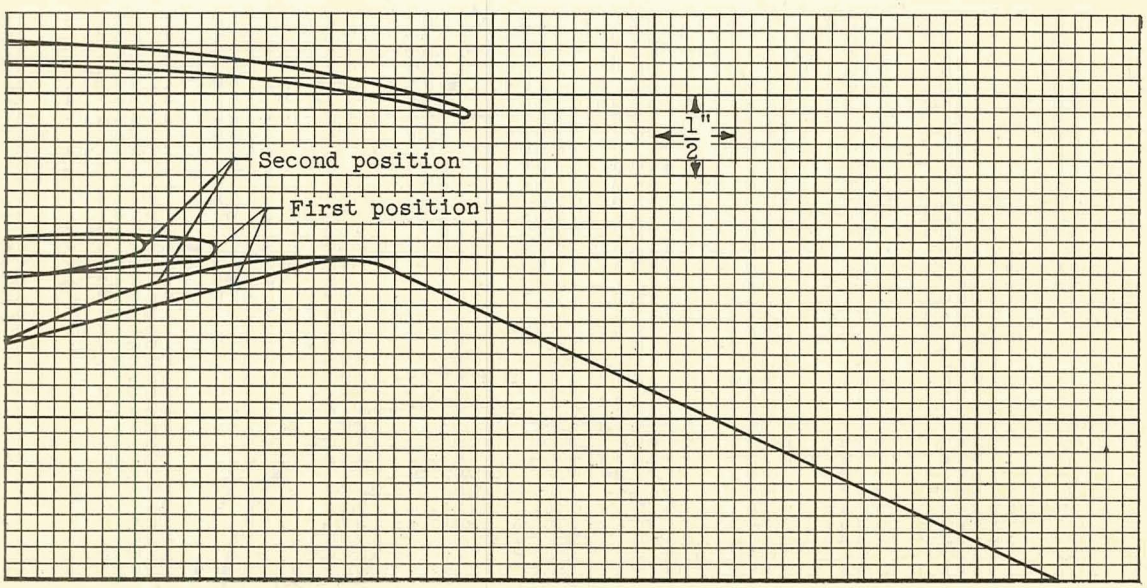

(c) Flush slot; cowl-lip parameter, 38°; slot gap (first and second positions), 0.200 inches.

Figure 4. - Concluded. Inlet-configuration details.

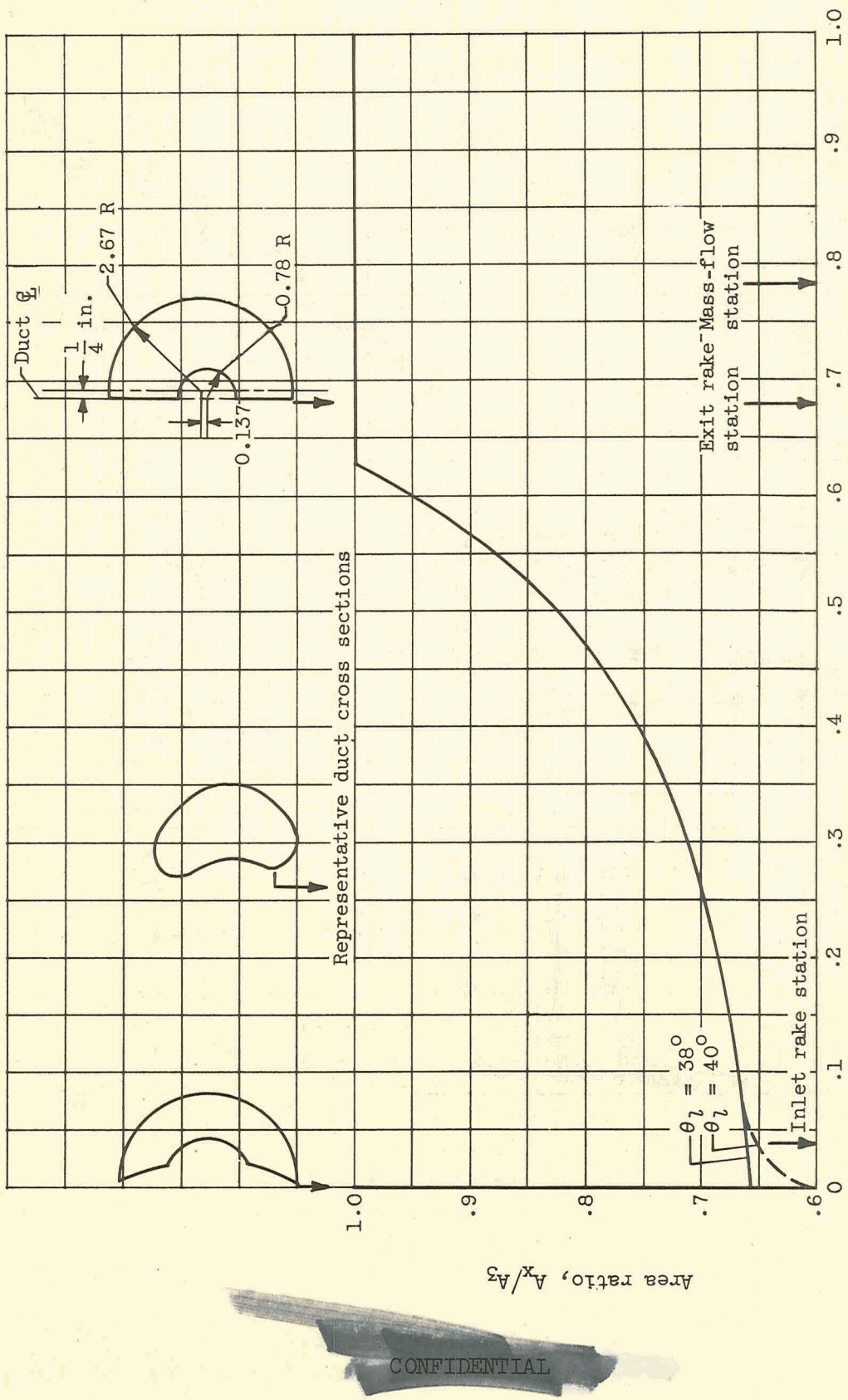

Figure 5. - Subsonic-diffuser area variation. Length of subsonic diffuser, 38.2 inches; diffuser-exit area, 0.161 square foot.

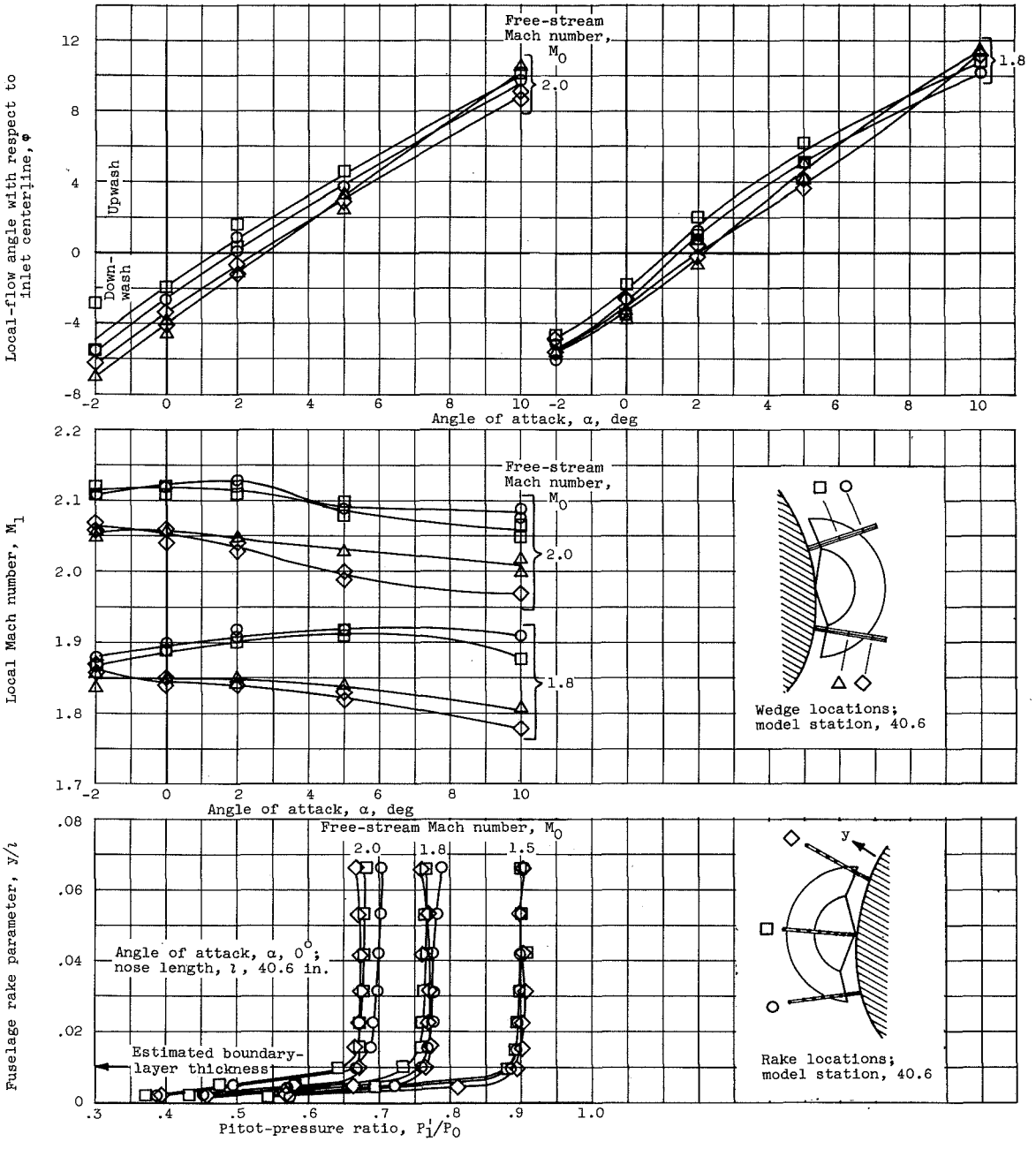

(a) With canopy.

Figure 6. - Flow conditions ahead of inlets.

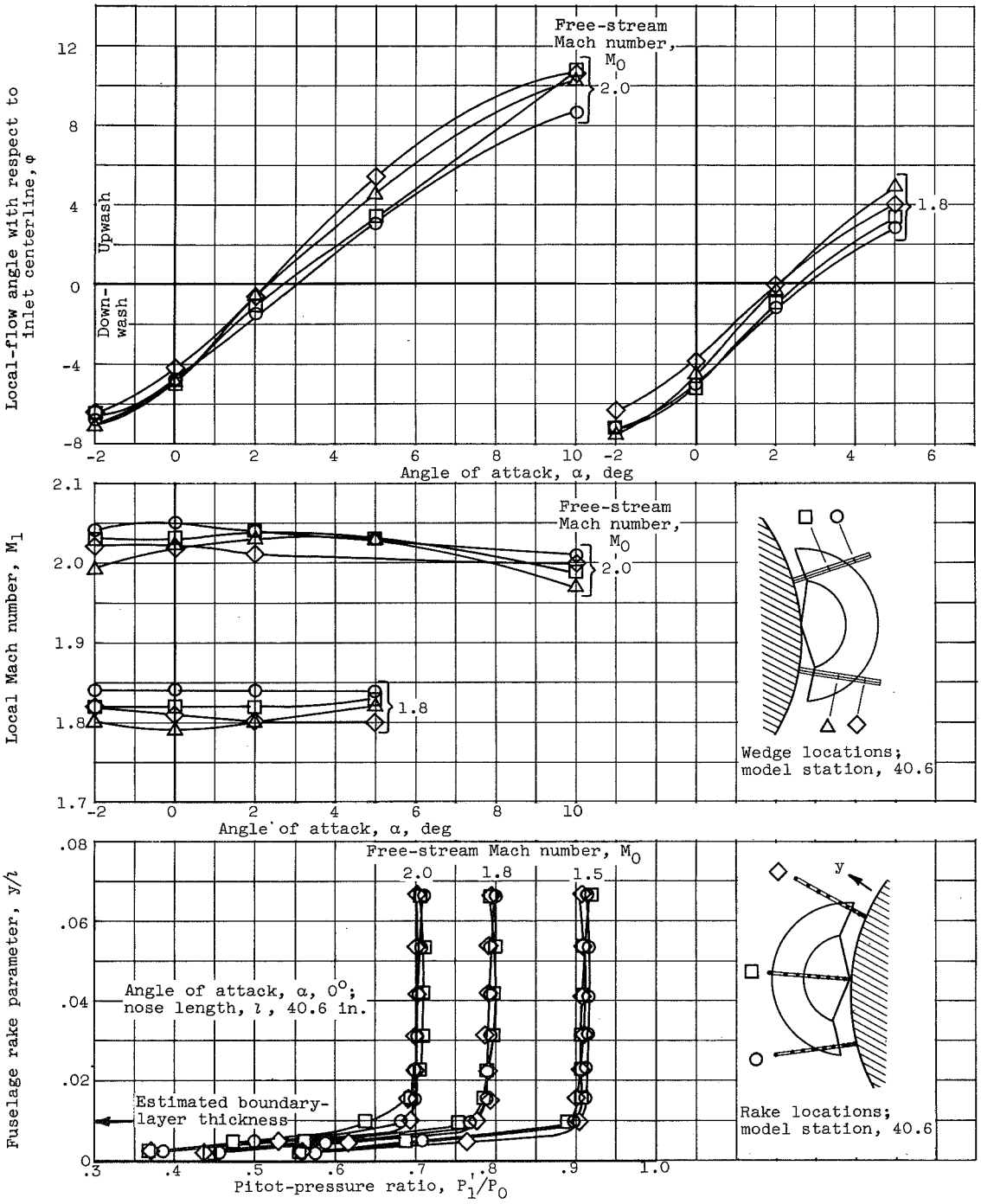

(b) Without canopy.

Figure 6. - Concluded. Flow conditions ahead of inlets.

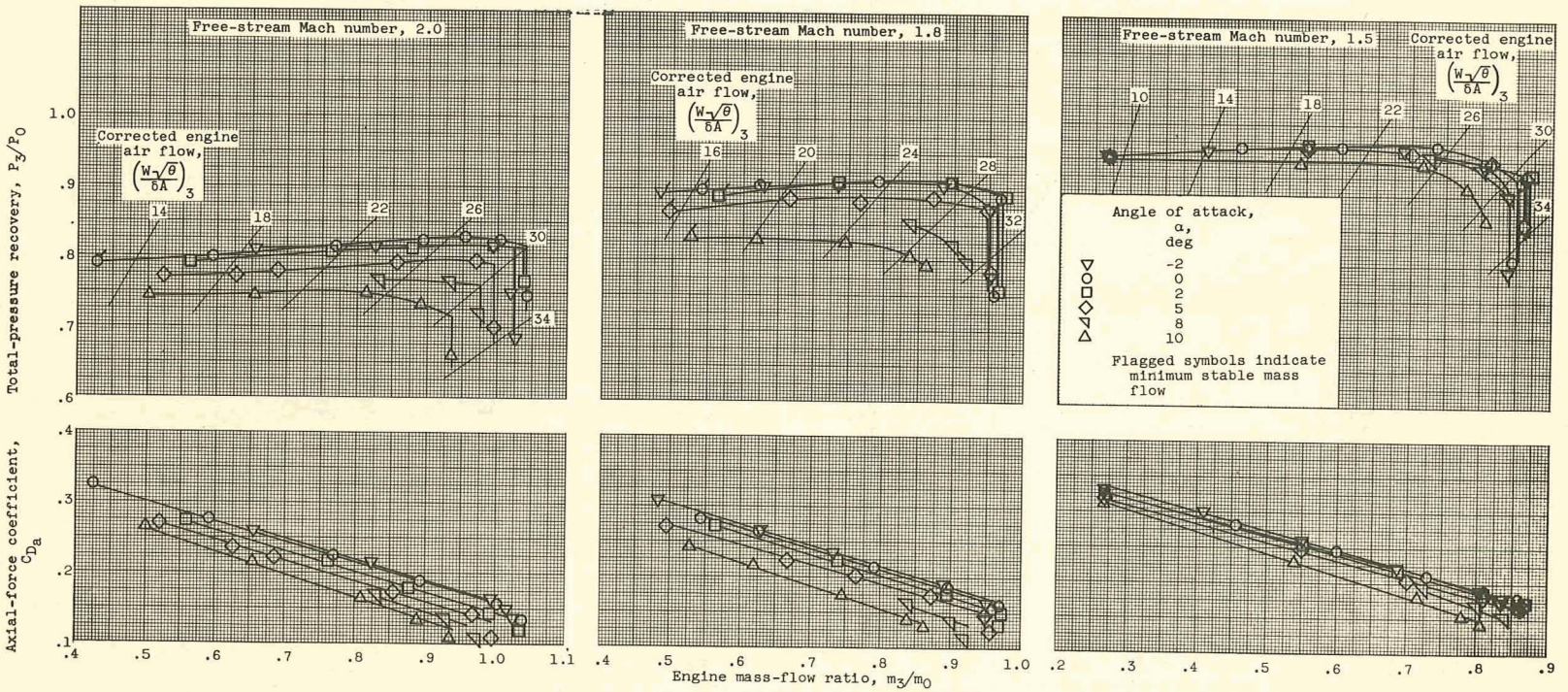

(a) No bleed inlet; cowl-lip parameter, 40°.

Figure 7. - Performance curves.

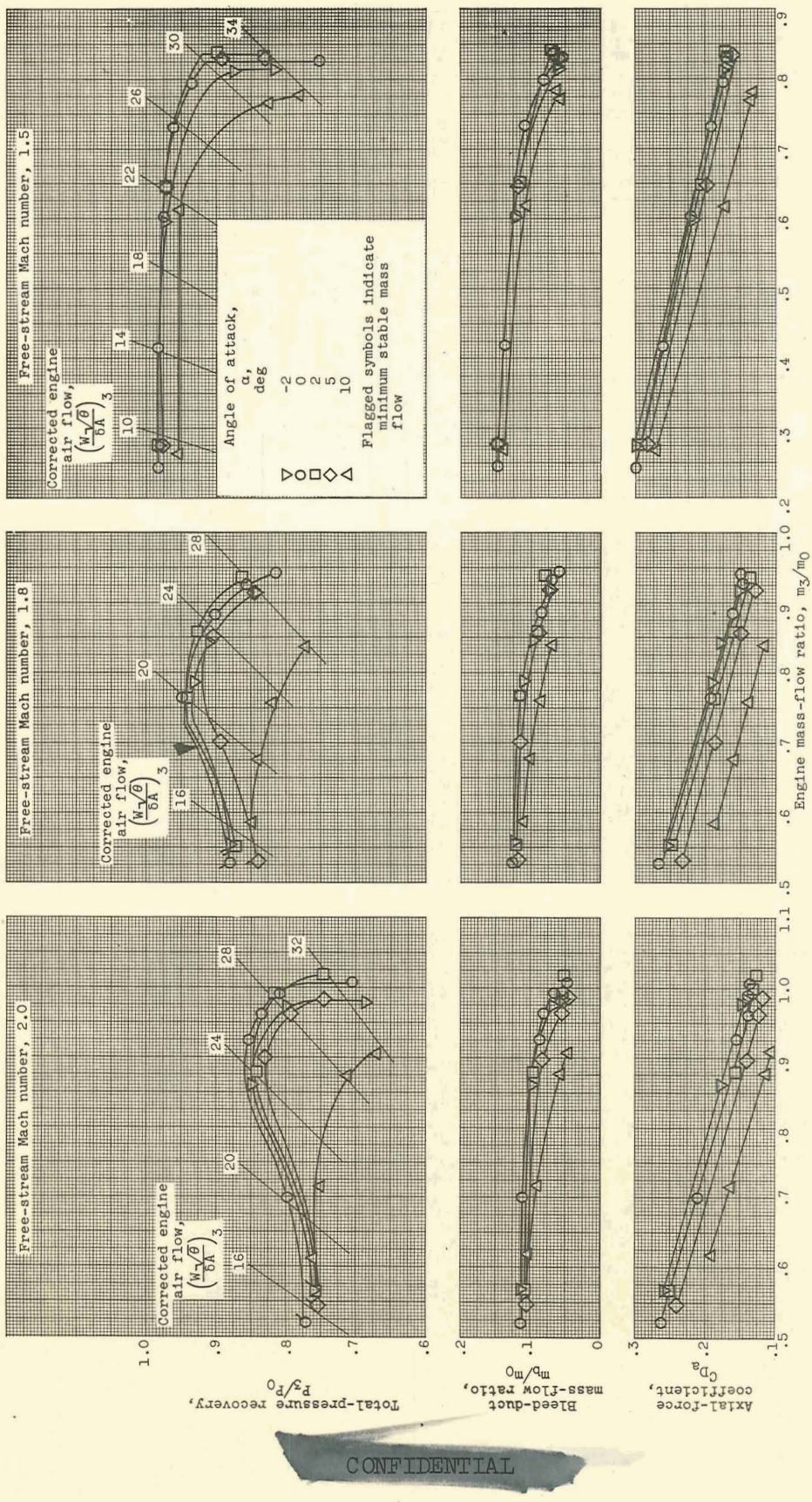

(b) Porous-surface bleed inlet; cowl-lip parameter, 40°.

Figure 7. - Continued. Performance curves.

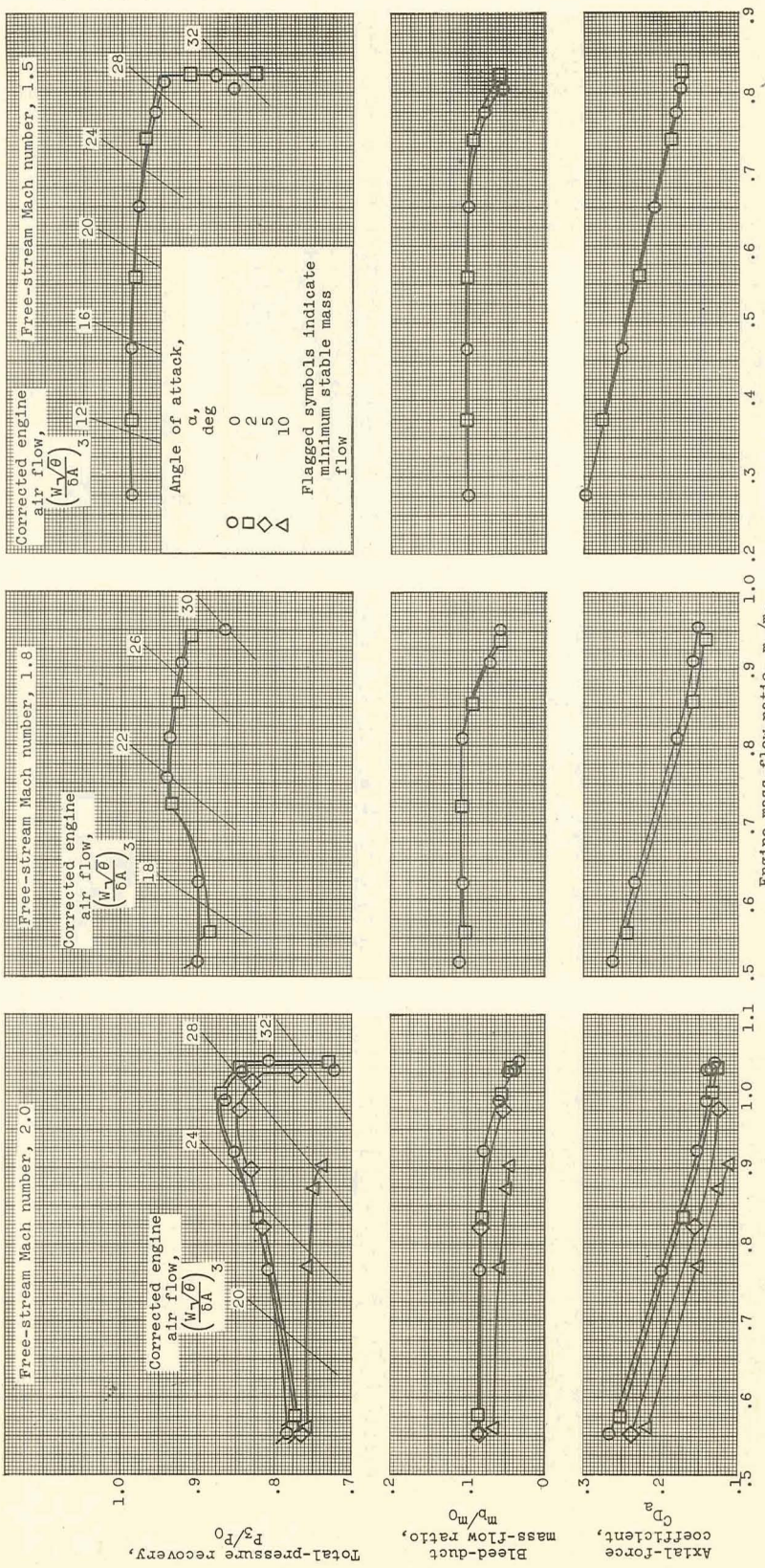

(c) Flush-slot inlet; cowl-lip parameter, 40°; bleed gap, 1/4 inch.

Figure 7. - Continued. Performance curves.

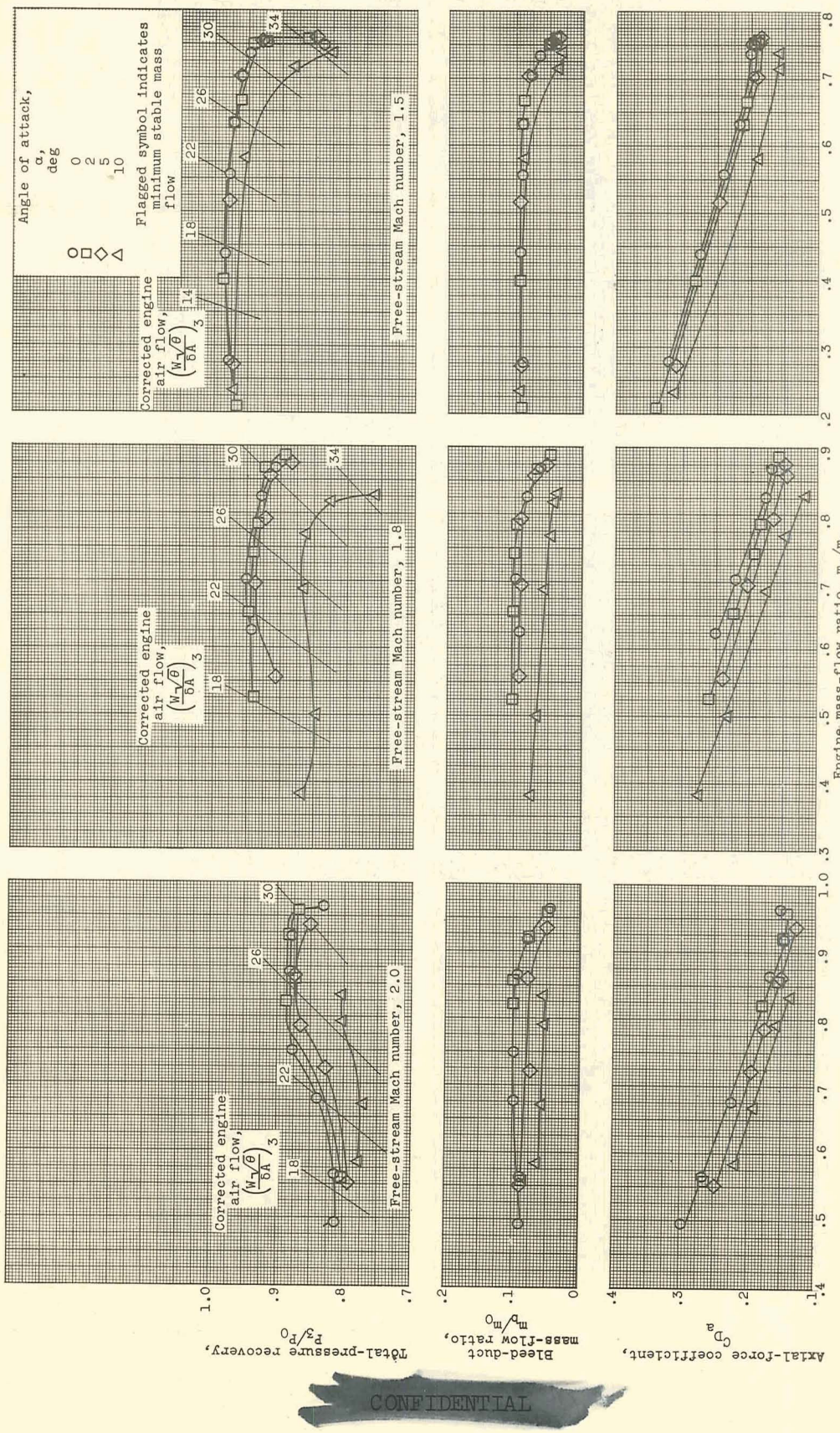

(d) Flush-slot inlet; first position; cowl-lip parameter, 38°.

Figure 7. - Concluded. Performance curves.

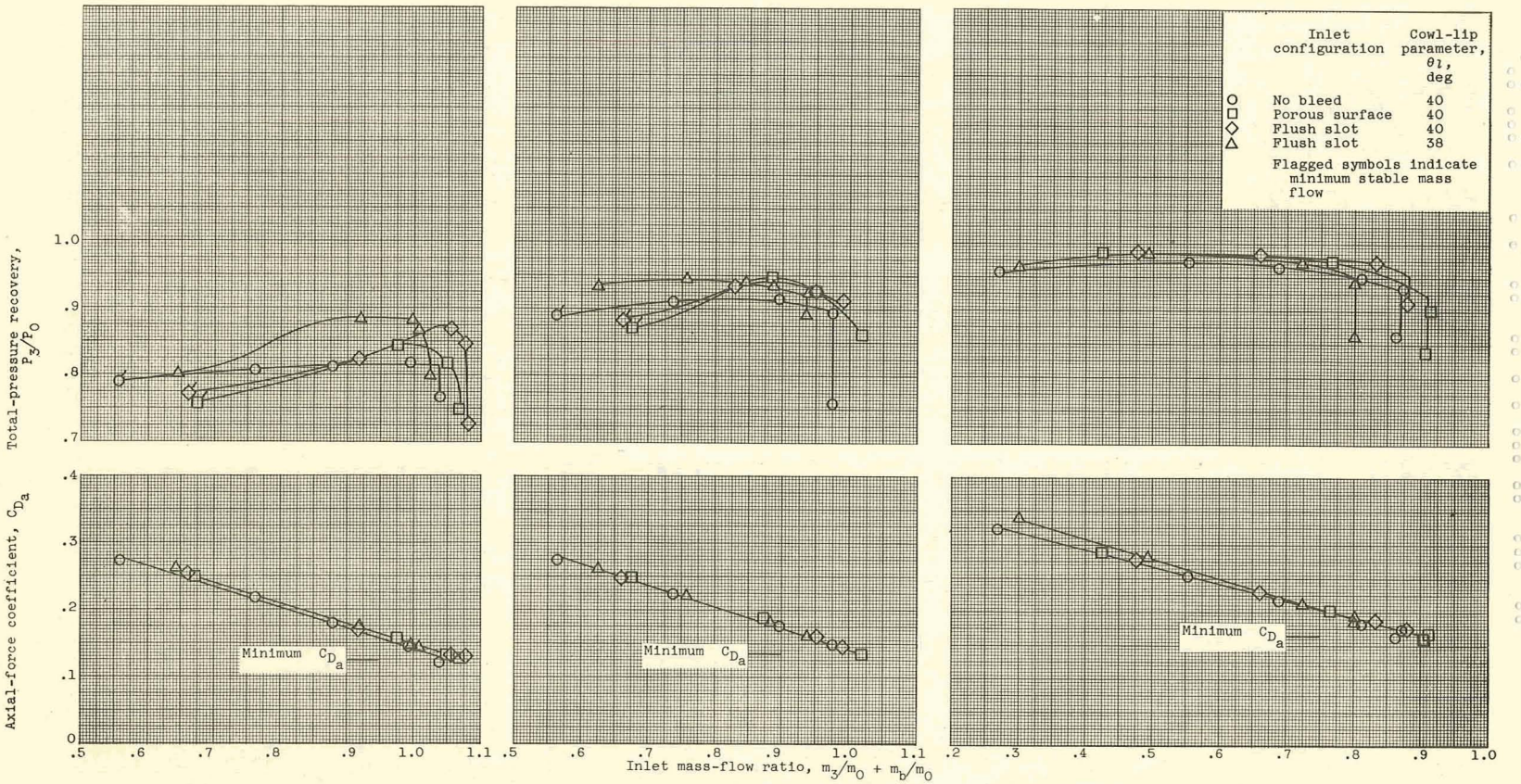

(a) Free-stream Mach number, 2.0. (b) Free-stream Mach number, 1.8. (c) Free-stream Mach number, 1.5.

Figure 8. - Inlet performance comparison; cruise angle of attack, 2°.

Figure 9. - Inlet comparison at cruise angle of attack of 2° and altitude of 35,000 feet.

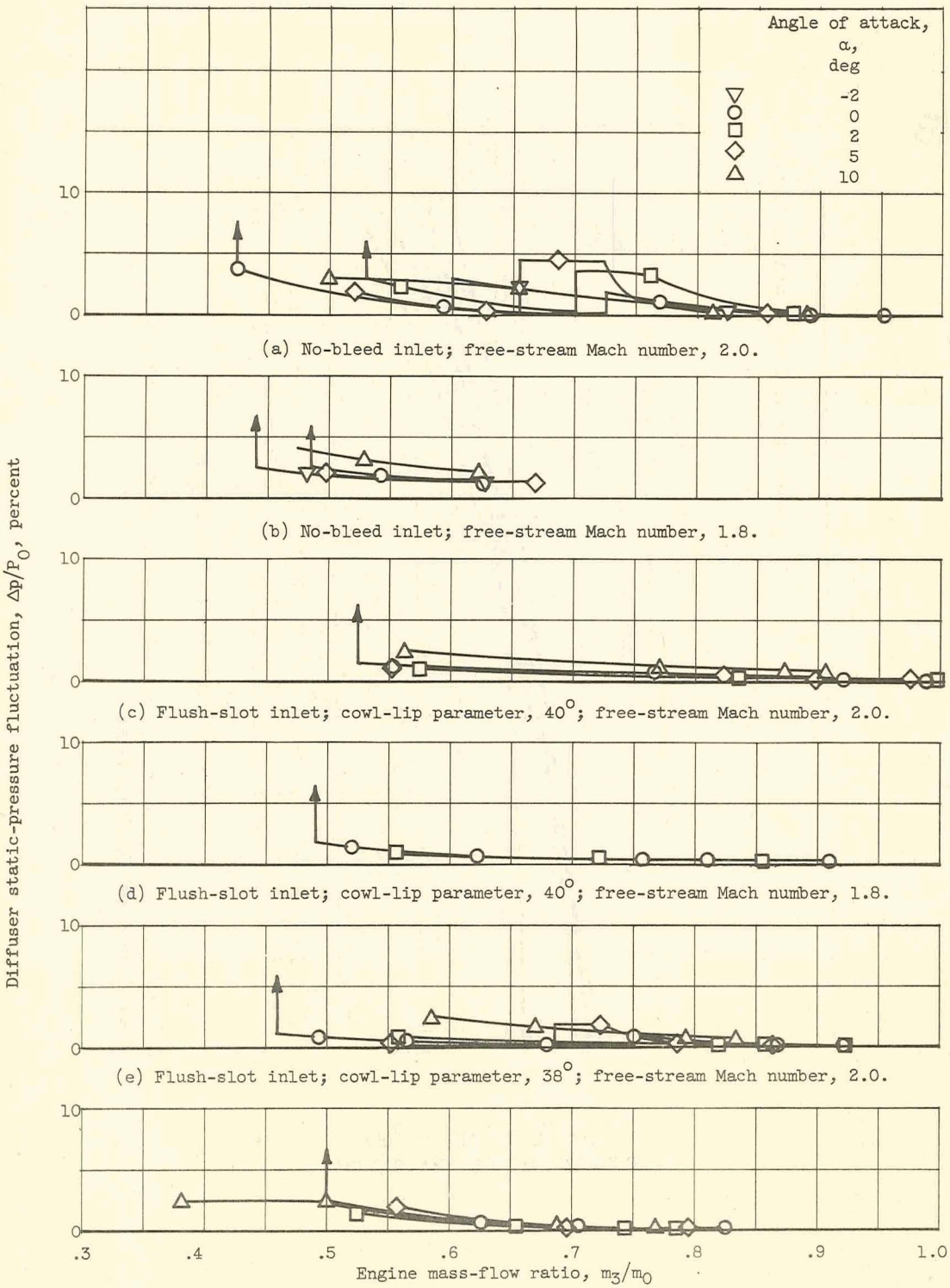

(a) No-bleed inlet; free-stream Mach number, 2.0.

(b) No-bleed inlet; free-stream Mach number, 1.8.

(c) Flush-slot inlet; cowl-lip parameter, 40°; free-stream Mach number, 2.0.

(d) Flush-slot inlet; cowl-lip parameter, 40°; free-stream Mach number, 1.8.

(e) Flush-slot inlet; cowl-lip parameter, 38°; free-stream Mach number, 2.0.

(f) Flush-slot inlet; cowl-lip parameter, 38°; free-stream Mach number, 1.8.

Figure 10. - Effect of internal bleed on diffuser static-pressure fluctuations.

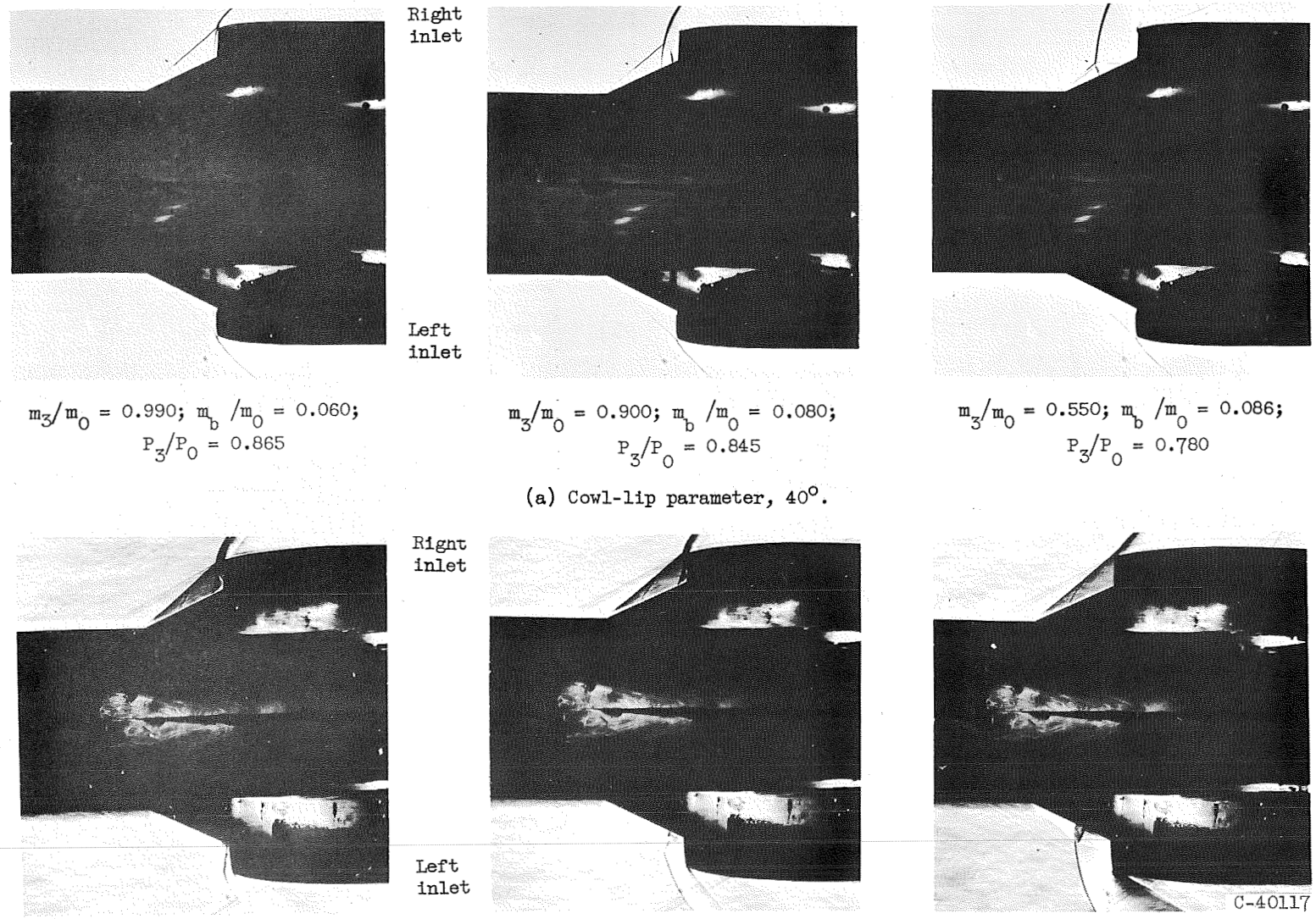

$m_3/m_0 = 0.990$; $m_b/m_0 = 0.060$; $P_3/P_0 = 0.865$

$m_3/m_0 = 0.900$; $m_b/m_0 = 0.080$; $P_3/P_0 = 0.845$

$m_3/m_0 = 0.550$; $m_b/m_0 = 0.086$; $P_3/P_0 = 0.780$

(a) Cowl-lip parameter, 40°.

$m_3/m_0 = 0.793$; $m_b/m_0 = 0.10$; $P_3/P_0 = 0.880$

$m_3/m_0 = 0.751$; $m_b/m_0 = 0.096$; $P_3/P_0 = 0.877$

$m_3/m_0 = 0.563$; $m_b/m_0 = 0.088$; $P_3/P_0 = 0.813$

(b) Cowl-lip parameter, 38°.

Figure 11. - Schlieren photographs at free-stream Mach number of 2.0.

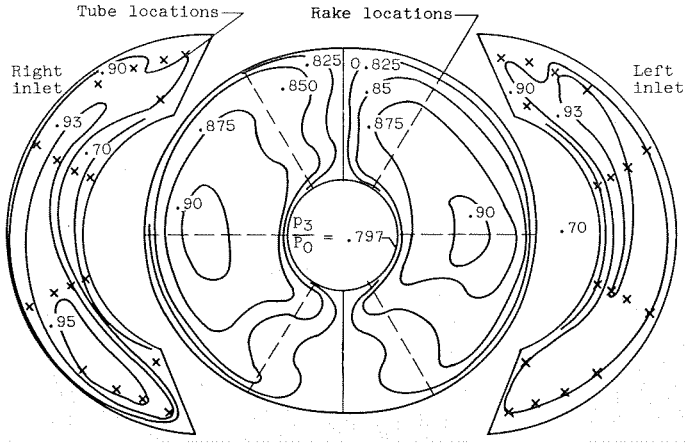

(a) $M_0 = 2.0$; $\alpha = 0^\circ$; $P_3/P_0 = 0.86$; $m_3/m_0 = 0.989$; $m_b/m_0 = 0.06$.

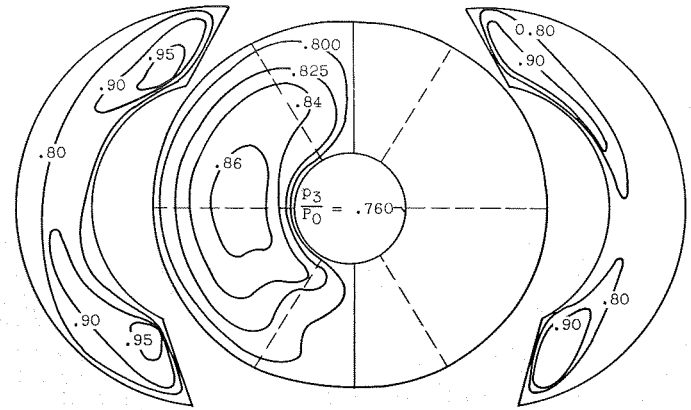

(b) $M_0 = 2.0$; $\alpha = 0^\circ$; $P_3/P_0 = 0.78$; $m_3/m_0 = 0.554$; $m_b/m_0 = 0.086$.

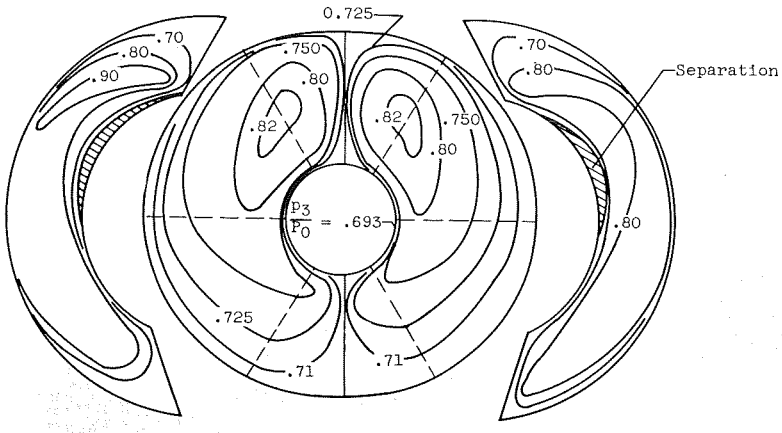

(c) $M_0 = 2.0$; $\alpha = 10^\circ$; $P_3/P_0 = 0.751$; $m_3/m_0 = 0.869$; $m_b/m_0 = 0.051$.

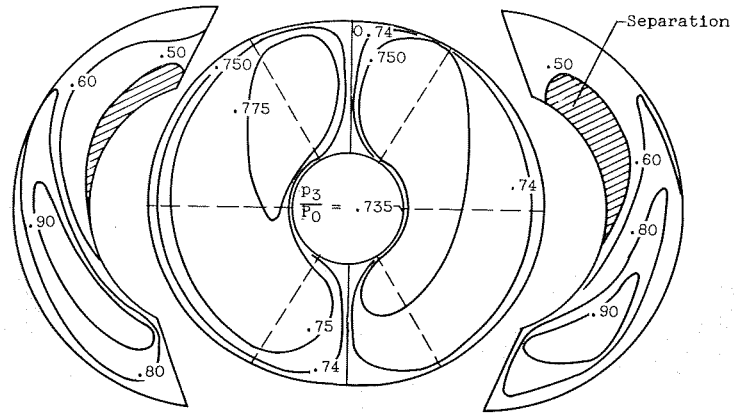

(d) $M_0 = 2.0$; $\alpha = 10^\circ$; $P_3/P_0 = 0.758$; $m_3/m_0 = 0.561$; $m_b/m_0 = 0.066$.

Figure 12. - Inlet and diffuser-exit total-pressure contours for flush-slot inlet; cowl-lip parameter, 40°.

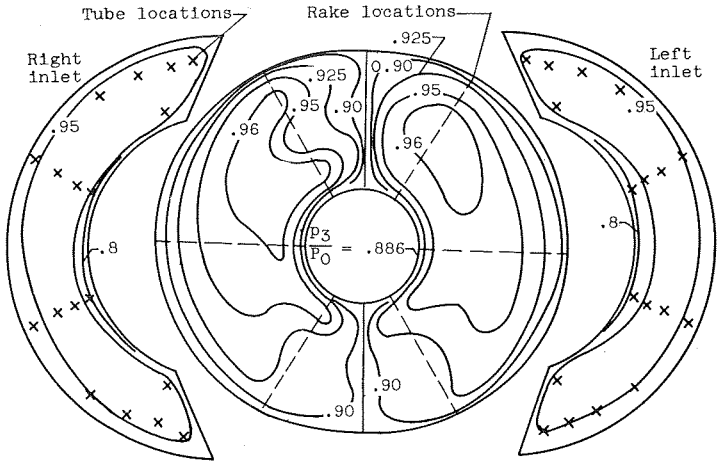

(e) $M_0 = 1.8$; $\alpha = 0^\circ$; $P_3/P_0 = 0.937$; $m_3/m_0 = 0.809$; $m_b/m_0 = 0.109$.

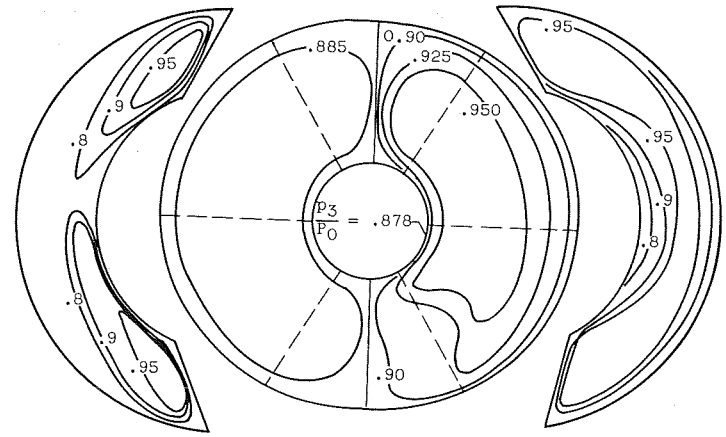

(f) $M_0 = 1.8$; $\alpha = 0^\circ$; $P_3/P_0 = 0.901$; $m_3/m_0 = 0.520$; $m_b/m_0 = 0.113$.

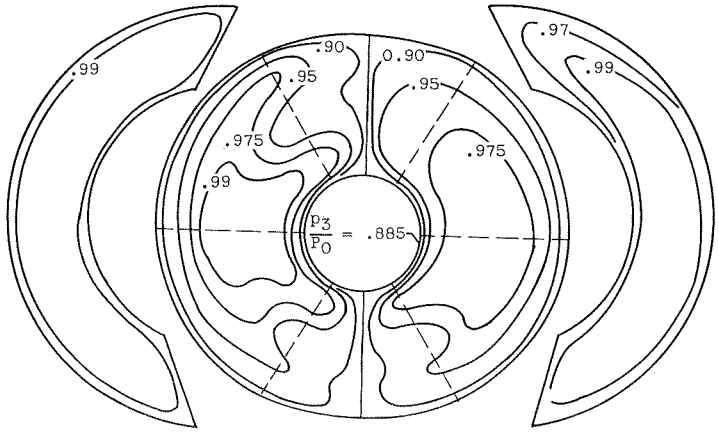

(g) $M_0 = 1.5$; $\alpha = 0^\circ$; $P_3/P_0 = 0.959$; $m_3/m_0 = 0.774$; $m_b/m_0 = 0.078$.

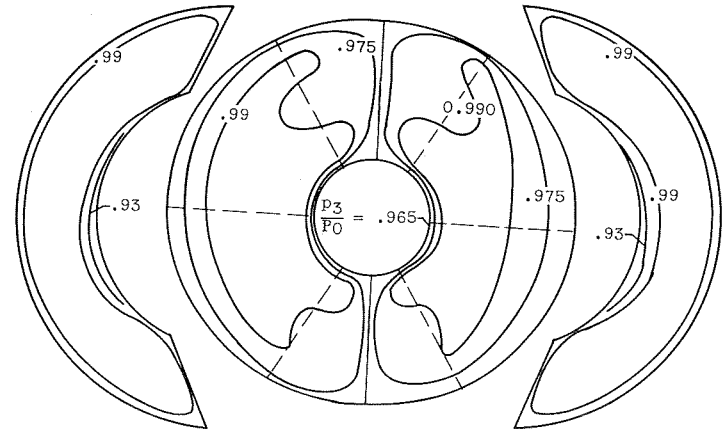

(h) $M_0 = 1.5$; $\alpha = 0^\circ$; $P_3/P_0 = 0.987$; $m_3/m_0 = 0.520$; $m_b/m_0 = 0.104$.

Figure 12. - Concluded. Inlet and diffuser-exit total-pressure contours for flush-slot inlet; cowl-lip parameter, 40°.

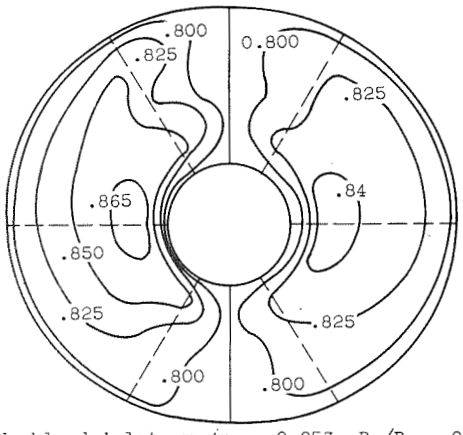

No-bleed inlet; $m_3/m_0 = 0.953$; $P_3/P_0 = 0.828$; $p_3/P_0 = 0.765$; maximum distortion, 9.1 percent.

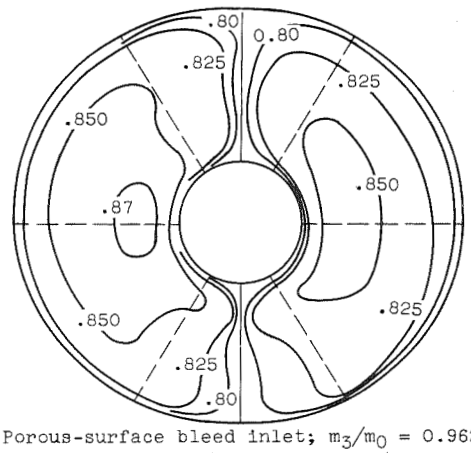

Porous-surface bleed inlet; $m_3/m_0 = 0.962$; $m_b/m_0 = 0.083$; $P_3/P_0 = 0.838$; $p_3/P_0 = 0.775$; maximum distortion, 7.8 percent.

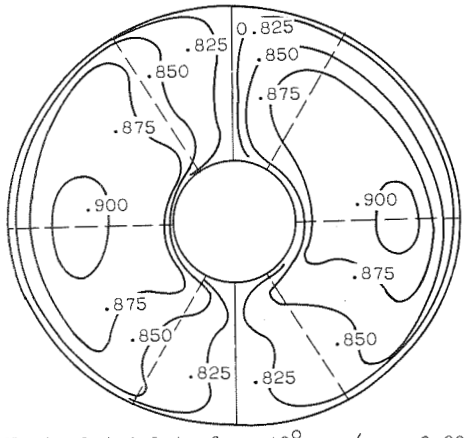

Flush-slot inlet; $\theta_l = 40^\circ$; $m_3/m_0 = 0.989$; $m_b/m_0 = 0.059$; $P_3/P_0 = 0.864$; $p_3/P_0 = 0.797$; maximum distortion, 9.0 percent.

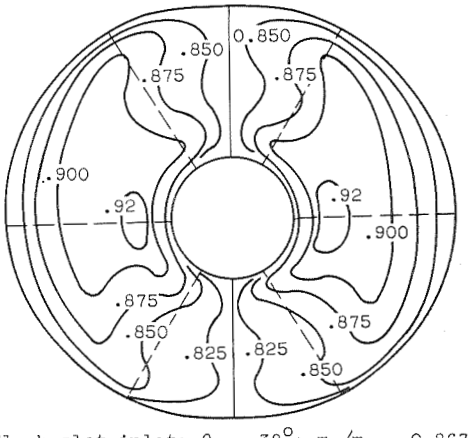

Flush-slot inlet; $\theta_l = 38^\circ$; $m_3/m_0 = 0.867$; $m_b/m_0 = 0.093$; $P_3/P_0 = 0.880$; $p_3/P_0 = 0.810$; maximum distortion, 11.4 percent.

(a) Corrected engine air flow, 26.6; zero angle of attack.

Figure 13. - Diffuser-exit total-pressure contours with and without bleed at Mach number, 2.0.

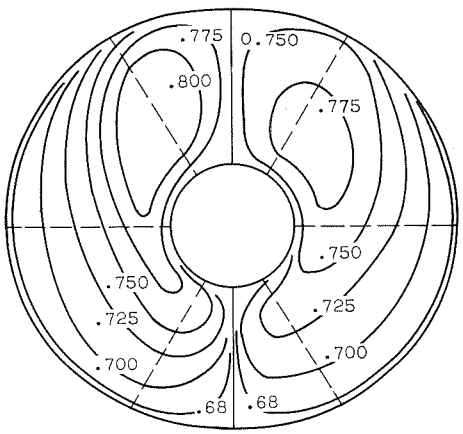

No-bleed inlet; m_3/m_0 = 0.891; P_3/P_0 = 0.731; p_3/P_0 = 0.670; maximum distortion, 17.1 percent.

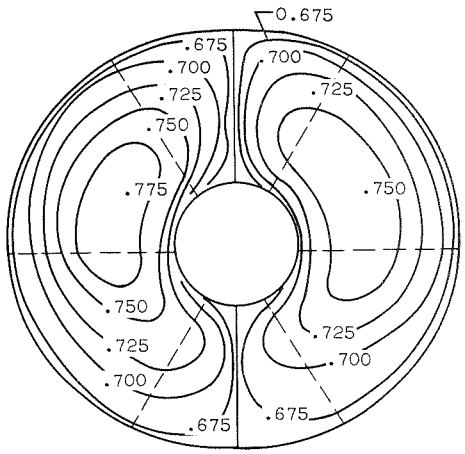

Porous-surface bleed inlet; m_3/m_0 = 0.878; m_b/m_0 = 0.058; P_3/P_0 = 0.714; p_3/P_0 = 0.653; maximum distortion, 17.2 percent.

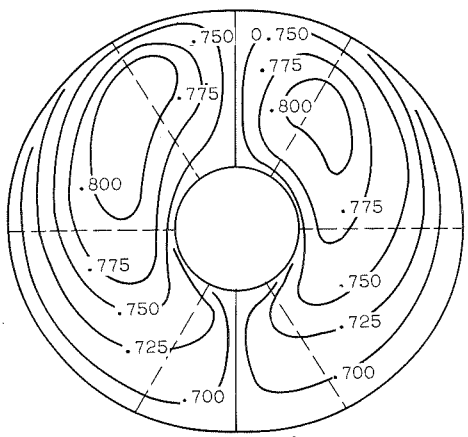

Flush-slot inlet; θ_l = 40°; m_3/m_0 = 0.905; m_b/m_0 = 0.047; P_3/P_0 = 0.738; p_3/P_0 = 0.672; maximum distortion, 18.3 percent.

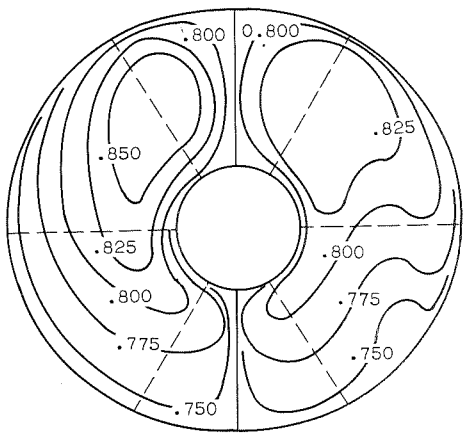

Flush-slot inlet; θ_l = 38°; m_3/m_0 = 0.834; m_b/m_0 = 0.054; P_3/P_0 = 0.803; p_3/P_0 = 0.680; maximum distortion, 14.3 percent.

(b) Corrected engine air flow, 28.2; angle of attack, 10°.

Figure 13. - Concluded. Diffuser-exit total-pressure contours with and without bleed at Mach number, 2.0.

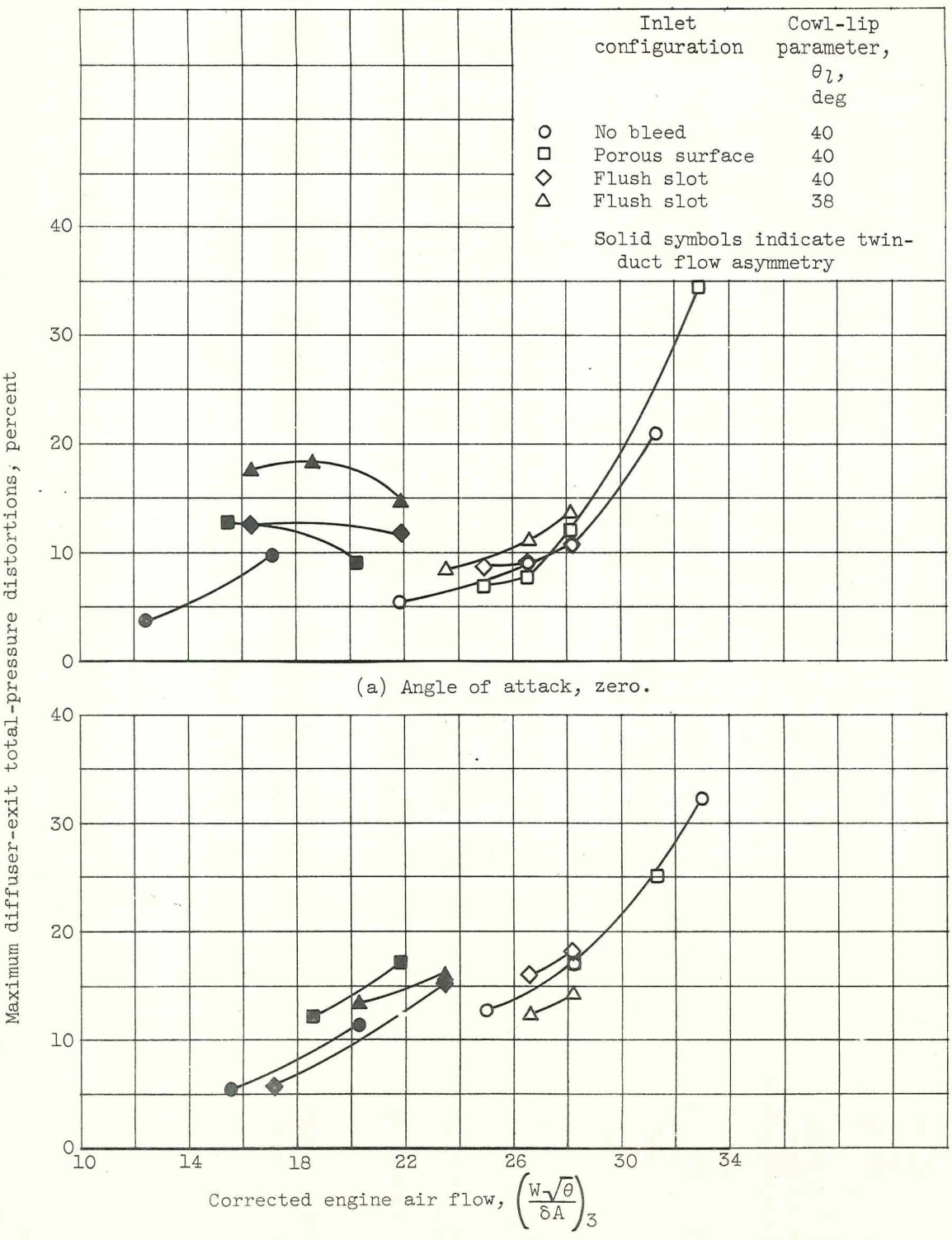

(a) Angle of attack, zero.

(b) Angle of attack, 10°.

Figure 14. - Diffuser-exit total-pressure distortions at Mach number, 2.0.

(a) Free-stream Mach number, 2.0; corrected engine air flow, 26.6.

(b) Free-stream Mach number, 1.8; corrected engine air flow, 23.5.

(c) Free-stream Mach number, 1.5; corrected engine air flow, 22.0.

Figure 15. - Effect of bleed-duct mass flow on performance of flush-slot inlet; cowl-lip parameter, 38°; zero angle of attack.

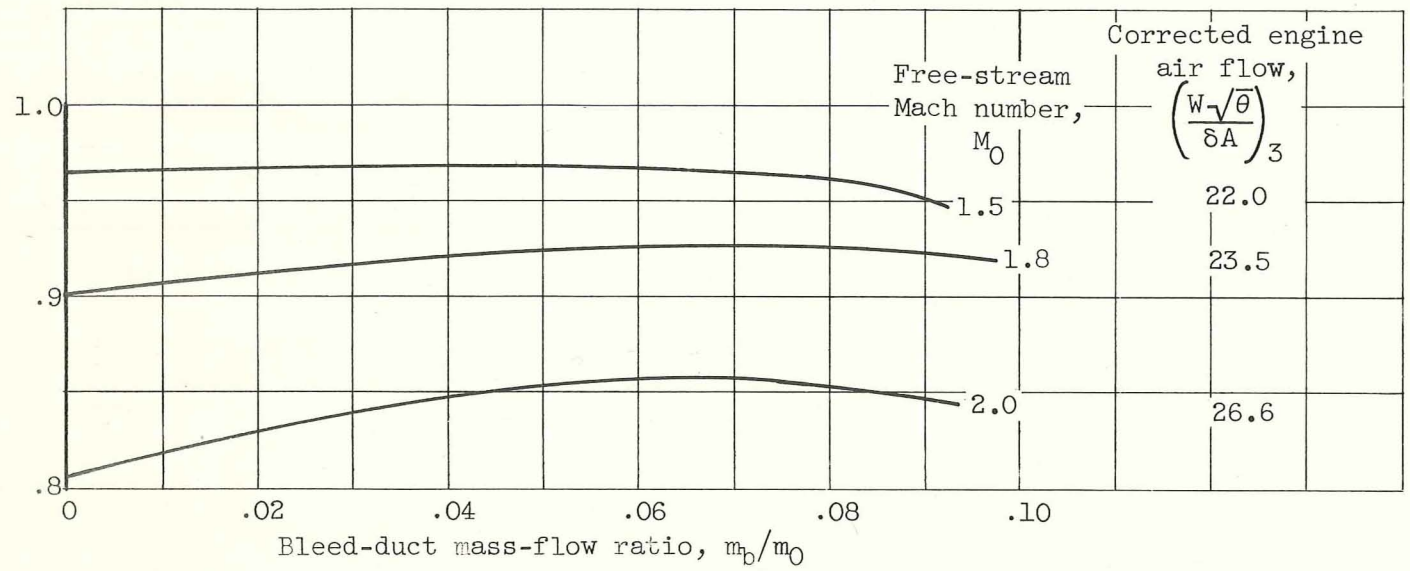

Figure 16. - Effect of bleed-duct mass flow on propulsive-thrust parameter of flush-slot inlet, with a cowl-lip parameter of 38°; angle of attack, zero; altitude of 35,000 feet.